1 Oxidation Resistance, Creep Strength and Room-Temperature Fracture Toughness of Mo–28Ti–

2 14Si–6C–6B Alloy

3

4 Tomotaka Hatakeyama[a,b,1], Alexander Kauffmann[b], Susanne Obert[b], Camelia Gombola[b], Martin

5 Heilmaier[b], and Kyosuke Yoshimi[a]*

6

7 [a] Department of Materials Science, Graduate School of Engineering, Tohoku University, 6-6-02,

8 Aramaki Aza Aoba, Aoba-ku, Sendai, 980-8579, Japan

9 [b] Institute for Applied Materials (IAM-WK), Karlsruhe Institute of Technology (KIT), Engelbert-

10 Arnold-Str. 4, 76131, Karlsruhe, Germany

11

12 *Corresponding author: Kyosuke Yoshimi

13 Phone and Fax: +81-22-795-7324

14 Email: yoshimi@material.tohoku.ac.jp

15 Tohoku University, 6-6-02 Aramaki Aza Aoba, Aoba-ku, Sendai, 980-8579, Japan.

16

[1] Present address: International Center for Young Scientists (ICYS), National Institute for Materials Science (NIMS), 1-2-1, Sengen, Tsukuba, Ibaraki, 305-0047, Japan

Abstract

A novel Mo–28Ti–14Si–6C–6B (atom %) alloy was designed for ultrahigh-temperature applications. Arc-melting and appropriate heat-treatment at 1600 °C results in the targeted four-phase microstructure comprising Mo_{ss}, Mo_5SiB_2 (T_2), Ti_5Si_3 and TiC. Previously developed three-phase alloys, comprising Mo_{ss}–T_2–Ti_5Si_3 and Mo_{ss}–T_2–TiC, are outperformed by this novel alloy as an adequate balance of oxidation resistance, creep strength and fracture toughness is attained: The oxidation behavior is characterized by substantial oxide scale formation at 1200 °C being accompanied by a mass loss of around -50 mg/cm^2 after 100 h of cyclic oxidation. The oxide scale is found to be composed of a top TiO_2 scale and an underlying duplex SiO_2/TiO_2 scale. Minimum creep rate of the alloy was in the order of 10^{-7} s^{-1} at 1200 °C and 300 MPa and its room-temperature fracture toughness was (12.8 ± 1.2) $MPa(m)^{1/2}$.

1. Introduction

As the efficiency of gas turbines and jet engines increases with increasing operating temperature, thermal barrier coating systems and cooling methods have been applied to Ni-based superalloys in order to permit higher turbine-inlet temperatures. However, these methods have led to efficiency losses in common and after all, the application of Ni-based superalloys is limited by the solvus temperatures of the strengthening phases [1,2]. Consequently, new ultrahigh-temperature materials with superior properties are required, especially with an increased inherent capability to withstand higher temperatures.

Mo–Si–B-based alloys are recognized as promising candidates for novel ultrahigh-temperature materials because of their high melting points and their good high-temperature strength properties [3–9]. The most important, but difficult, challenge in applying such alloy systems is the achievement of an appropriate combination of creep strength, fracture toughness and oxidation resistance [3].

Recently, Miyamoto et al. investigated the effect of adding TiC to Mo–Si–B alloys. They developed the so-called 1st generation Mo–Si–B–TiC alloy with a composition of Mo–10Ti–5Si–10C–10B (atom %) [10]. The constituent phases of this alloy are Mo solid solution (Mo_{ss}), Mo_5SiB_2 (T_2), TiC and a small amount of Mo_2C [10–12]. The alloy has a density of less than 9 g/cm^3 [10] and exhibits excellent high-temperature strength [10,13,14], as well as adequate room-temperature fracture toughness [15]. However, it does not possess an adequate oxidation resistance at elevated temperatures. Significant mass loss caused by volatilization of Mo oxide (MoO_3) is observed due to an insufficient Si content (of only 5 atom %) [16,17]. An increase in the Si content is essential for the formation of an oxidation-resistant protective oxide layer. However, merely increasing the Si content results in changes in phase equilibria and a transformation of a proportion of ductile Mo_{ss} into Mo_3Si [18], leading to a decrease in room-

1 temperature fracture toughness.

2 Another method to improve the material properties of Mo–Si–B-based alloys is macro-

3 alloying with Ti in order to stabilize M_5Si_3-type silicides. Thermodynamic calculations suggest

4 that tetragonal Mo_5Si_3 ($D8_m$ structure, T_1) or hexagonal Ti_5Si_3 ($D8_8$ structure) are stabilized

5 instead of Mo_3Si [19–22]. Schliephake et al. investigated the creep strength and oxidation

6 resistance of Mo–Si–B–Ti alloys (Mo–9Si–8B–29Ti and Mo–12.5Si–8.5B–27.5Ti (atom %)) that

7 contained $(Ti,Mo)_5Si_3$ [23,24]. These alloys showed a superior creep strength and a much lower

8 density compared to Ni-based superalloys and other Mo–Si–B-based alloys.

9 More recently, Hatakeyama et al. investigated the phase equilibria of a Si-rich Mo–Si–

10 B–Ti–TiC alloy system. They obtained a microstructure consisting of Mo_{ss}, T_2, Ti_5Si_3 and TiC at

11 a composition of Mo–28Ti–14Si–6C–6B (atom %) [17]. This alloy yields a low density of only

12 7.4 g/cm^3, a competitive high-temperature compressive strength and room-temperature fracture

13 toughness in combination with an improved oxidation resistance at 800 and 1100 °C compared

14 with the 1st generation Mo–Si–B–TiC alloy [17,25]. In order to assess the ability of the new alloy

15 to operate at very high temperatures, we have studied its oxidation resistance, creep strength and

16 fracture toughness in detail.

17

18 **2. Materials and methods**

19 The Calphad software *Pandat* (version 2018) with the database *PanMo2018a* was used

20 to predict the solidification route and the composition of each constituent phase in Mo–28Ti–

21 14Si–6C–6B (atom %).

22 Samples of the Mo–28Ti–14Si–6C–6B alloy were prepared by the arc-melting

23 technique under an Ar atmosphere. Button ingots were prepared by using the following raw

24 materials: Mo (99.99 mass %), Si (99.99 mass %), B (99 mass %), Ti (99.95 mass %) and TiC (99

mass %). The ingot was flipped and remelted several times to ensure its homogeneity. After casting, the ingots were homogenized at 1600 °C for 24 hours and then cooled in the furnace under an Ar atmosphere. The heat-treated buttons were cut by electro-discharge machining (EDM).

The constituent phases of the heat-treated alloy were identified by X-ray diffraction (XRD) using the Cu-Kα radiation. The microstructure of the heat-treated alloy was characterized by scanning electron microscopy (SEM) with an accelerating voltage of 15 kV in the backscatter electron (BSE) mode and electron backscatter diffraction (EBSD) based orientation imaging microscopy (OIM) with an accelerating voltage of 25 kV. The specimen surface for EBSD–OIM was finished by vibratory polishing using a diamond slurry with an average particle size of 40 nm. The volume fraction of the constituent phases was determined by image analysis of BSE micrographs. The concentrations of Mo, Ti, and Si in the heat-treated alloy were determined semi-quantitatively for each phase by SEM–energy-dispersive X-ray spectrometry (SEM–EDS) with the Mo-Lα, Ti-Kα, and Si-Kα lines with an accelerating voltage of 15 kV.

Cyclic oxidation tests were carried out with the specimens measuring $5 \times 5 \times 4$ mm^3 at 800, 1100, and 1200 °C for up to 100 hours in box furnaces. The tests were divided into three periods: (i) twenty 1 h cycles, (ii) six 5 h cycles, and finally (iii) five 10 h cycles. Three specimens were prepared for each tested temperature and for each test duration of 1, 10, and 100 hours. The specimens were ground to P2500 to remove the layer of contamination produced by EDM. The oxidized specimens were embedded in resin and ground to the substrate to show their cross-sections. The cross-sections were then polished and analyzed by SEM and SEM-EDS.

Compression creep tests were performed at 1200, 1250 and 1300 °C with applied stresses of 100, 200 and 300 MPa in a vacuum of better than 1.15–1.18×10^{-3} mbar with samples of $3 \times 3 \times 5$ mm^3 in size. The faces in contact with the punches were carefully ground to P2500

1   in a parallel holder to ensure a parallel geometry perpendicular to the compression axis and to

2   remove the layers of contamination produced by EDM. The punches were made of SiC and

3   lubricated with boron nitride.

4   Elastic parameters of the heat-treated alloy were measured by the electromagnetic

5   acoustic resonance (EMAR) method using samples of $5 \times 5 \times 5$ mm^3 in size. Details of the EMAR

6   measurements and analysis are presented elsewhere [26].

7   Three-point bending tests on the heat-treated alloy were performed at room temperature

8   by using a chevron-notched $(5 \times 5 \times 25)$ mm^3 sample geometry as employed by Schneibel et al.

9   [27] and Yang et al. [28]. The shape of the notch is described by Moriyama et al. as 'Test-3' [15].

10 The tests were conducted three times at a cross-head speed of 10 μm/s with an Instron 5982

11 machine. The fracture toughness was evaluated by applying the following Irwin's similarity

12 relationship:

13
$$K_Q = (GE')^{1/2} = \left(\frac{U}{A} \cdot \frac{E}{1 - v^2} \right)^{\frac{1}{2}} \qquad (1)$$

14 Here, $G = U/A$ is calculated from the energy U absorbed during the fracture of an area A swept

15 out by the crack, and $E' = E/(1-v^2)$ is the plane-strain Young's modulus, E is the Young's modulus,

16 and v is the Poisson ratio [27,28].

17

18 **3. Results and discussion**

19 3.1. Thermodynamic prediction and microstructural characterization

20   Fig. 1 shows the molar phase fractions in the Mo–28Ti–14Si–6C–6B (atom %) alloy as

21 calculated by the *Pandat* software. The vertical dashed lines indicate the liquidus temperature

22 (2368 °C), the heat treatment temperature (1600 °C) and the temperature for complete

23 decomposition of Mo$_3$Si into Mo$_{ss}$ and Mo$_5$Si$_3$ (1239 °C). According to these thermodynamic

24 predictions, the TiC phase solidifies primarily at around 2370 °C followed by the solidification of

the T_2 phase at about 2100 °C. With further decreasing temperature down to 2000 °C, a sudden drop of the phase fraction of the liquid phase is predicted as a result of the formation of Mo_{ss} and Mo_3Si. The volume fractions of the resulting phases do not change significantly at temperatures down to 1250 °C. Below this temperature, Mo_3Si decomposes into Mo_{ss} and Mo_5Si_3. Finally, a phase equilibrium of Mo_{ss}, T_2, Mo_5Si_3 and TiC is achieved. Hence, the decomposition of Mo_3Si leads to an increased volume fraction of ductile Mo_{ss}. It should be noted that the formation of the Mo_{ss}–Ti_5Si_3 eutectic and of a small volume fraction of a Mo_3Si phase as found in the as-cast Mo–28Ti–14Si–6C–6B alloy [17,25] is not observed in these calculations.

Figs. 2(a) and (b) show a BSE image and an XRD pattern, respectively, of the cast and subsequently heat-treated (1600 °C for 24 hours) Mo–28Ti–14Si–6C–6B alloy. The upper and lower sides in the micrograph are corresponding to the top and bottom sides of the button ingot, respectively. The phases generated were (i) dendritic Mo_{ss}, (ii) dendritic TiC, (iii) vertically elongated Mo_5SiB_2 (T_2) and (iv) Ti_5Si_3, the last of which co-exists with Mo_{ss} in a lamellar, presumably eutectic microstructure. This four-phase constitution indicates that, the Mo_3Si phase present in the as-cast state decomposes into Mo_{ss} and hexagonal Ti_5Si_3 upon heat-treatment at 1600 °C, rather than tetragonal Mo_5Si_3, as suggested by the thermodynamic calculations. The (110) reflection at 23.87° and the (200) reflection at 27.63° in the XRD pattern support the formation of hexagonal Ti_5Si_3. Schliephake et al. have previously reported that the Ti_5Si_3 phase is stable over Mo_5Si_3 in alloys with similar high Ti contents [23].

In summary, we therefore obtained a Mo_{ss}–T_2–Ti_5Si_3–TiC four-phase equilibrium, which represents a combination of phases within the previously reported Mo–Si–B–TiC (Mo_{ss}–T_2–TiC) [10] and Mo–Si–B–Ti (Mo_{ss}–T_2–Ti_5Si_3) alloys [23].

Fig. 3 shows inverse pole figure (IPF) maps for each phase. These reveal that Mo_{ss} and TiC grow as rather large single-crystalline dendrites. A similar single-crystalline growth is also

1 found for plate-like T_2. In the case of Mo_{ss}, orientation changes within the dendrites (visible as

2 color gradients) indicate the existence of geometrically necessary dislocations and/or subgrains.

3 While coherent twin boundaries were frequently observed in TiC phases in the 1st generation Mo–

4 Si–B–TiC alloy [11], twin boundaries were not found in the present case. The Ti_5Si_3 phase exists

5 as a Mo_{ss}–Ti_5Si_3 eutectic. In the eutectic region, the Ti_5Si_3 phase appears to be the matrix due to

6 its penetrating network structure while the Mo_{ss} phase seems to be a dispersed phase.

7   The volume fraction and composition of the constituent phases obtained both,

8 experimentally and theoretically are summarized in Figs. 4(a) and 4(b). In this study, the light

9 elements B and C were ignored due to insufficient accuracy of the EDS analyses. The given

10 compositions were normalized in relation to the total amount of Mo, Ti and Si. The

11 thermodynamically calculated compositions were normalized in the same way. The volume

12 fractions of the phases were calculated by using the values obtained at 1239 °C, where the

13 decomposition of Mo_3Si to Mo and Mo_5Si_3 was complete, with the density and the formula weight

14 of stoichiometric Mo, T_2, Mo_5Si_3 and TiC. The predicted compositions correspond to that at

15 1600 °C (the heat treatment temperature) for Mo_{ss}, T_2 and TiC phase, and 1239 °C for the Mo_5Si_3

16 phase. The experimentally determined volume fractions of Mo_{ss}, T_2, Ti_5Si_3 and TiC are 40.9, 24.1,

17 29.7 and 5.3 vol %, respectively. A good agreement with thermodynamic prediction is obtained;

18 remarkably, the volume fraction of M_5Si_3 silicides is similar, even though the predicted crystal

19 structure of the silicide differs from that determined experimentally.

20   According to the EDS results, the Mo_{ss} contains about 18.4 ± 0.6 atom % Ti and $1.3 \pm$

21 0.6 atom % Si. 30.8 ± 0.5 atom % Ti is dissolved in T_2 according to this analysis and 22.8 ± 1.8

22 atom % Mo is dissolved in Ti_5Si_3. In contrast, the thermodynamic calculations indicate that the

23 solubility of Mo in the hexagonal Ti_5Si_3 is only ~12.5% [20]. This underestimation of the

24 solubility and/or the positive effect on the stability of the interstitial atoms (B and C) for the $D8_8$

1 structure [29] could cause the difference in the structural stability of the M_5Si_3 silicides. By

2 considering the stoichiometric composition of these intermetallic compounds, it becomes

3 apparent that Ti mainly replaces Mo on its sites in the Mo_5SiB_2 phase, whereas Mo mainly

4 replaces Ti in the Ti_5Si_3 phase. It is found that TiC contains about 8 atom % Mo and a negligible

5 amount of Si. For comparison, the composition of the TiC phase in 1st generation Mo–Si–B–TiC

6 alloy was reported to be 23.5Mo–31.0Ti–45.5C (atom %) [11], which correspondingly contains a

7 much higher proportion of Mo. These differences in the Mo/Ti ratio in TiC phase can be

8 understood by the phase equilibria between Mo_{ss} and TiC in Mo–Ti–C ternary system [30]. As a

9 positive effect of the off-stoichiometry and Mo substitution in TiC on the fracture toughness was

10 presented by Moriyama [15], the off-stoichiometry and Mo substitution in TiC in the present alloy

11 might also be non-negligible in relation to its mechanical properties. Apart from the Mo_5Si_3

12 silicide, the composition of each phase determined by EDS shows a good agreement with the

13 thermodynamic predictions. However, the concentrations of solute elements are consistently

14 underestimated: the Ti concentration in Mo_{ss} was determined to be $18.4 \pm 0.6\%$ by EDS, but

15 12.4% by calculation, the Mo concentration in TiC was determined to be $7.9 \pm 0.4\%$ by EDS, but

16 1.3% by calculation. The error bar represents the standard deviation of the measured points. Here,

17 the distribution of Mo in the TiC phase at 2368 °C (the liquidus temperature of the alloy) was

18 calculated to be about 5.8% and that of Ti in Mo_{ss} at the solvus temperature of the alloy (2009 °C)

19 was about 15.3%. The experimentally obtained compositions of TiC and Mo_{ss} are rather close to

20 the predicted value at the liquidus and solvus temperatures, but not at the heat treatment

21 temperature, suggesting sluggish diffusion of these elements or the existence of nanosized

22 precipitates of TiC in the Mo_{ss} phase and of Mo_{ss} in the TiC phase, as previously reported for Mo–

23 Si–B–Ti–C systems [15,16]. Another possibility on this underestimation is the insufficient

24 accuracy of the calculation, because the calculated equilibria do not follow the tie line in

1   experimentally determined Mo–Ti–C ternary phase diagram [30].

2

3   3.2. Oxidation behavior

4   Fig. 5 shows the mass-change kinetics observed during cyclic oxidation of the Mo–

5   28Ti–14Si–6C–6B alloy in air at 800, 1100 and 1200 °C. The isothermal oxidation kinetics of the

6   1st generation Mo–Si–B–TiC alloy (with no added Ti_5Si_3) obtained at 1100 °C [16] are shown for

7   comparison. At 800 °C, the Mo–28Ti–14Si–6C–6B alloy shows a small gain in mass within the

8   first hour, which subsequently turns into a mass loss with ongoing cyclic oxidation. Note that this

9   mass loss is mainly attributed to continuous sublimation of MoO_3, but the overall mass change

10   also includes the gain in mass caused by the formation of solid SiO_2 or TiO_2. The alloy exhibits

11   catastrophic oxidation behavior, as the sample was almost completely oxidized after 100 h of

12   cyclic oxidation, which is observed for many other Mo-based silicides and referred to as pesting

13   phenomenon [31–33]. At 1100 °C, the mass loss is much smaller than that obtained at 800 °C and

14   also less severe compared to the 1st generation alloy. At 1200 °C, the mass-change kinetics is

15   similar to those observed at 1100 °C up to 40 h, but then deviates in the later stages of the

16   oxidation test in form of rather linear kinetics.

17   Fig. 6 shows cross-sections of Mo–28Ti–14Si–6C–6B alloy oxidized at 1100 °C (left

18   side) and 1200 °C (right side) for 1, 10 and 100 h. At 1100 °C, the oxidation progresses mainly in

19   the dendritic Mo_{ss} phase as indicated by the deep trenches at the former locations of Mo_{ss},

20   especially during the early stages of oxidation. In contrast, thin scales are formed on the other

21   phases after the first hour of oxidation. After 10 h of cyclic oxidation, the growth of the oxide

22   seems to be retarded on the T_2 phase. In addition, regions of non-oxidized Ti_5Si_3 phase are

23   frequently found in the oxide scale. We assume that Mo_{ss} is selectively oxidized in the eutectic

24   regions of Mo_{ss}–Ti_5Si_3. This indicates an enhanced oxidation resistance for the Ti_5Si_3 phase, as

1   recently demonstrated in Refs. [16,34,35]. However, spallation was observed on the top of the

2   oxide layer over the entire surface as highlighted in the image for 10 h at 1100 °C. This indicates

3   inadequate adhesion and results in an insufficiently dense oxide scale. After the 100 h of oxidation,

4   the thickness of the oxide layer is more homogeneous and its average thickness is about (218 ±

5   18) μm. The error bar represents the standard deviation of the measured oxide thickness. The

6   oxide layer mainly consists of a TiO_2/SiO_2 duplex layer (mixed light and dark gray in Fig. 6) with

7   partially exists dense TiO_2 layer (light gray in Fig. 6) near the surface. The formation of the top

8   TiO_2 layer near the edges of the sample is disturbed as indicated in the inset to Fig. 6. In contrast

9   to the observations at 10 h, spallation of the oxide is not observed after 100 h, indicating an

10   increasing steadiness of the oxide.

11   At 1200 °C, a similar retarded oxidation of the T_2 phase is found, whereas the Ti_5Si_3 in

12   the surface-near eutectic regions completely oxidizes in comparison with oxidation at 1100 °C.

13   Unlike at 1100 °C, spallation of the scale did not occur at 1200 °C after 10 h. Instead, a dense

14   TiO_2 layer is formed on top of the underlying TiO_2/SiO_2 duplex layer. After 100 h of oxidation,

15   the average thickness of the oxide layer is (224 ± 38) μm, almost the same as at 1100 °C.

16   Interestingly, the thickness of the outermost TiO_2 layer was (22 ± 7) μm, which is markedly greater

17   than that observed at 1100 °C. In addition, large pores are formed in the oxide layer at 1200 °C.

18   Fig. 7(a) shows the BSE image of a cross-section of the alloy oxidized at 1200 °C for

19   100 h, together with the corresponding EDS elemental mappings in Figs. 7(b) to (e). The

20   mappings confirm the formation of a rather dense TiO_2 layer on top of a TiO_2/SiO_2 duplex layer,

21   which contains large pores. The interfaces of each oxide layer are traced by white lines. In Fig.

22   7(b), small amounts of oxygen are detected at the substrate adjacent to the duplex oxide layer,

23   implying internal oxidation. Focusing on Fig. 7(c), it is seen that about half the duplex layer

24   consists of Si oxide. The Si oxide is accounted for some contribution to the oxidation resistance

1 at 1200 °C. Since the formation of Si oxide results from the consumption of T_2 and/or Ti_5Si_3, a

2 slower oxidation of Ti_5Si_3 regions at 1100 °C might decrease the oxidation resistance compared

3 to that at 1200 °C. This implies, as previously claimed for the Mo–Si–B ternary alloy system [36],

4 that fine Ti_5Si_3 regions provide better oxidation resistance through formation of a SiO_2 layer at

5 high temperatures. Mo was not detected throughout the oxidized area, as shown in Fig. 7(e). This

6 means that Mo completely oxidized to MoO_3 at the oxide/substrate interface and immediately

7 evaporated outwards through the oxide layer. This implies that the oxide layer permits rapid

8 transport of gases, including oxygen. Thus, while the oxidation resistance of the alloy is improved

9 compared to the 1st generation Mo–Si–B–TiC alloy, it was still inadequate, because the resulting

10 oxide scale was not sufficiently protective, especially at 800 °C. As confirmed in Fig. 5,

11 continuous evaporation of MoO_3 obviously occurred during the exposure. Schliephake et al.

12 pointed out that the evaporation of MoO_3 disturbs the formation of an oxide scale and the

13 disturbance is much more significant at lower temperatures because of the slow kinetics of oxide

14 scale formation [37]. Because the activity of the elements in the constituent phases influences the

15 kinetics of oxide formation, lowering the concentration of Mo in each phase and thus lowering

16 the degree of MoO_3 volatilization might improve the oxidation resistance of this alloy system

17 [25,35,37–40].

18

19 3.3. Creep strength

20   Fig. 8(a) shows the creep strain versus time curves obtained from two compression creep

21 tests performed at 1300 °C and a stress of 300 MPa. The tests were stopped when the logarithmic

22 strains reached 12% and 50% to observe the microstructure just after exhibiting the minimum

23 creep rate and on the accelerating stage with high creep damage, respectively. The tests showed a

24 typical creep behavior, including transient creep and acceleration. Fig. 8(b) shows the strain rate

1　on a logarithmic scale versus strain curves. The minimum creep rates were 6.3×10^{-6} s^{-1} and 3.9

2　$\times 10^{-6}$ s^{-1}, respectively, as indicated by the horizontal dashed lines in the figure. As the difference

3　between these values was within one order of magnitude, a good reproducibility of the creep

4　testing is confirmed in this study. Figs. 8(c) and 8(d) display BSE images of the microstructures

5　after creep compression to logarithmic strains of (c) 12% and (d) 50%, respectively. The

6　compression direction is horizontal in these micrographs. Although it is difficult to identify

7　macroscopic differences between the initial microstructure and that shown Fig. 8(c), small cracks

8　were observed in T_2 as indicated by white arrowheads in the figure. Unlike in Fig. 8(c), a

9　significantly deformed primary Mo_{ss} phase as well as Mo_{ss}–Ti_5Si_3 eutectic regions are observed

10　in Fig. 8(d). In addition, a cracked T_2 phase region is more prominent in Fig. 8(d). These results

11　suggest that at the transient stage, T_2 phase dominates the compressive creep strength. However,

12　once cracks are introduced in T_2 phase, the internal stress is decreased, resulting in the

13　acceleration by the plastic deformation of primary Mo_{ss} and Mo_{ss}–Ti_5Si_3 eutectic regions.

14　　　Fig. 9(a) and 9(b) show the creep-strain versus time curves obtained from the

15　compression creep tests (a) at 1200–1300 °C and 300 MPa and (b) at 1300 °C and 100–300 MPa.

16　All tests were interrupted when the creep strain reached about 12–15%. Figs. 9(c) and 9(d) depict

17　the strain-rate versus creep-strain curves corresponding to Figs. 9(a) and 9(b), respectively. The

18　minimum creep rates decrease with decreasing testing temperature or applied stress. Fig. 9(e) is

19　an Arrhenius plot of the minimum creep rate at an applied stress of 300 MPa; the apparent

20　activation energy (Q) was calculated to be 639 kJ/mol. Fig. 9(f) displays a Norton plot at 1300 °C

21　and the stress exponent (n) was determined to be 2.7. Creep parameters related to high-

22　temperature deformation of Mo–Si–B-based alloys have been collected and summarized by

23　Kamata et al. [14]. The reported apparent activation energies for creep scatter between 234 and

24　730 kJ/mol while the reported stress exponents are in the range from 2.0 to 5.5; therefore, the two

values obtained in the present study fall within these reported ranges. Because these parameters are significantly influenced by small differences in the composition and volume fractions of the constituent phases, it is difficult to discuss their physical meanings in the current situation. Nevertheless, the activation energy was close to that of monolithic Ti_5Si_3 (620–640 kJ/mol [41]), implying a significant contribution from Ti_5Si_3 to the deformation. This hypothesis is supported by the significantly deformed Ti_5Si_3 grains shown in Fig. 8(d).

In Fig. 10, the minimum creep rate of the Mo–28Ti–14Si–6C–6B alloy at 1200 °C is compared with those of other Mo–Si–B alloys and the single-crystal Ni-based superalloy CMSX-4 as a function of density-normalized applied stress. Because this temperature is close to the solvus temperature of the γ' phase in CMSX-4, the creep strength of CMSX-4 is markedly inferior to those of the Mo–Si–B-based alloys [42]. The creep strength of the Mo–28Ti–14Si–6C–6B alloy is greater than that of the ternary Mo–Si–B alloys [6] and is similar to that reported for a Mo–9Si–8B–29Ti alloy, which consists of Mo_{ss}, T_2 and Ti_5Si_3 phase in volume fractions of 61.1%, 29.2%, and 9.4% [23]. It is well known that the creep strength of Mo–Si–B-based alloys deteriorates with increasing volume fraction of the Mo_{ss} phase [43]. However, the Mo–9Si–8B–29Ti and Mo–28Ti–14Si–6C–6B alloys have similar strengths, even though the former contains a much higher volume fraction of Mo_{ss} phase. Larger volume fraction of T_2 phase, which is supposed to be dominating the creep strength at the transient stage, and the solid solution strengthening by larger amounts of solute elements in Mo_{ss} (26.1 atom % Ti and 2.3 atom % Si [23]) might lead to a higher strength per volume fraction of Mo_{ss} phase in the Mo–9Si–8B–29Ti alloy.

3.4. Room-temperature fracture toughness

At RT, the Young's modulus and the Poisson's ratio of the alloy determined by the

EMAR method are 299 GPa and 0.265, respectively. The Young's modulus is lower by about 16% than that of the 1st generation Mo–Si–B–TiC alloy (358 GPa) [15]. Due to the proportionality of square route of the Young's modulus and fracture toughness, this difference results in a toughness lower by about 9%, if other parameters are considered unchanged. The Poissons ratio was barely changed by Ti enrichment and incorporation of Ti_5Si_3 [15]. Fig. 11 shows the load-displacement curves of the heat-treated Mo–28Ti–14Si–6C–6B alloy in three-point bending tests to determine the fracture toughness. Absorbed energy U in eq. (1) is obtained by integrating a load-displacement curve. From these curves, the room-temperature fracture toughness is determined to be (12.8 ± 1.2) MPa(m)$^{1/2}$. The error bar represents the standard deviation of the evaluated fracture toughness. This value is higher than that of a Mo–28Ti–14Si–6C–6B alloy heat-treated for 24 hours at 1800 °C (11.4 MPa(m)$^{1/2}$ [17]), which has the same constituent phases with similar volume fractions but heat-treated 200 °C higher than the conditions in the present study. Conversely, this value is lower than that of the 1st generation Mo–Si–B–TiC alloy (15.2 MPa(m)$^{1/2}$), which was also prepared by arc-melting and homogenization at 1800 °C for 24 hours [15]. Moriyama et al. pointed out that the fracture toughness of the 1st generation Mo–Si–B–TiC alloy shows a good linear relationship with the volume fractions of Mo_{ss} + TiC [15] and that the fracture toughness of the Mo–28Ti–14Si–6C–6B reference alloy homogenized at 1800 °C was in good agreement with this relationship [17]. However, the fracture toughness of the Mo–28Ti–14Si–6C–6B alloy changed with the heat treatment temperature, even though the volume fraction of Mo_{ss} and TiC phases are hardly affected by the heat treatment conditions. Due to the dominant role of Mo_{ss} for fracture toughness of Mo–Si–B-based alloys by ductile-phase toughening, the change in the ductility of the Mo_{ss} phase by changing the solute-atom content should be considered. It is well known that Si decreases the ductility of the Mo_{ss} phase [44]. By considering the Mo–Si binary phase diagram [45], a lower annealing temperature permits a reduction in the

1   solute Si content of the Mo_{ss} phase. EDS analysis showed that the Si content in samples of the

2   Mo_{ss} phase of the Mo–28Ti–14Si–6C–6B alloy heat-treated at 1600 and 1800 °C were 1.3 and

3   2.8 atom %, respectively [17]. Therefore, the lower annealing temperature might decrease the

4   dissolved Si content in Mo_{ss} phase and leads to a better room-temperature fracture toughness.

5   Fig. 12 shows BSE micrographs of fracture surfaces of the alloy after bending tests for

6   the (a) lowest and (c) highest fracture toughness values in this study. Figs. 12(b) and 12(d) are

7   higher magnification images of the regions highlighted in Figs. 12(a) and 12(c), respectively. As

8   can be seen in Figs. 12(a) and 12(b), more than half of the area of the fracture surface is comprised

9   of coarse flat T_2 regions, the fracture toughness of which is reported to be only about 2 $MPa(m)^{1/2}$

10   in single crystalline form [46]. The T_2 exhibits transgranular fracture, suggesting preferential

11   propagation of cracks in T_2. In contrast, in Figs. 12(c) and (d), a ductile Mo_{ss} phase appeared to

12   occupy a moderate area fraction of the fracture surface as dendritic grains or a lamellar eutectic

13   with Ti_5Si_3, indicating a sufficient contribution of Mo_{ss} to a ductile-phase toughening mechanism

14   [47]. This results in better fracture toughness. These differences arise from an inhomogeneous

15   distribution of the plate-shaped T_2 phase formed during the casting process [11]. Figs. 12(a) and

16   12(c) show that the plate extended widely in the ingot, in the order of 1 mm in size. According to

17   Fig. 1, the T_2 phase forms in the early stages of solidification, and its nucleation is independent

18   of other solid phases within an interval of about 100 K gap until the formation of subsequent

19   solidification products starts. While the dendritic form of most metallic solid solutions is triggered

20   by constitutional super-cooling at the diffuse solidification front, the plate-shape morphology of

21   T_2 is a result of fast-growing crystallographic planes at comparably sharp solid-liquid interfaces.

22   The situation of de-coupled T_2 formation is unlike the solidification process of Mo_{ss}–T_2–TiC alloy

23   (without Ti_5Si_3), where the growth of T_2 is spatially restricted by other phases: most of T_2 forms

24   in the later stage of solidification through eutectic reactions of liquid (L) → Mo_{ss} + T_2 + TiC (or

1   Mo_2C) or by the reaction $L + Mo_2B \rightarrow Mo_{ss} + T_2$ [48], resulting in the formation of finer T_2 of

2   about 10 μm in size [49]. From the microstructure of the alloy shown in Fig. 2(a), the average

3   spacing of T_2 plates is estimated to be approximately 50–100 μm and the width of each plate is

4   tens of microns. In addition, T_2 tends to elongate along the solidification direction as shown in

5   Fig. 2(a). By considering this T_2 distribution, cleavage of the coarsened T_2 should be unavoidable.

6   When a crack tip approaches the T_2 plate, the crack propagates across the plate, resulting in low

7   energy absorption. If the angle between the cracking direction and T_2 plate is close to

8   perpendicular, the geometry might help to gain absorbed energy by crack deflection. From these

9   considerations, the following two ideas are suggested as methods for enhancing the room-

10   temperature fracture toughness: (i) microstructure refinement of the T_2 phase to disperse the

11   preferential transgranular failure and (ii) control of the solidification microstructure, i.e.

12   preferential growth of the T_2 phase to avoid the parallelism between the longitudinal direction of

13   T_2 plates and the crack-propagation direction. Furthermore, a finely distributed T_2 phase should

14   help to avoid cracking during creep deformation and should enhance the supply of Si to the oxide

15   layer by scarifying itself.

16   Fig. 13(a) shows the room-temperature fracture toughness values of various Mo–Si–B-

17   based alloys as a function of the volume fraction of Mo_{ss} [3,15]. The plot for the 1st generation

18   Mo–Si–B–TiC alloy is indicated as 'TiCp'. As can be seen from this figure, these plots have a

19   slightly positive tendency, which supports the mechanism of ductile-phase toughening [47] by a

20   Mo_{ss} phase. The toughness obtained in this study is relatively high from the viewpoint of its Mo_{ss}

21   volume fraction, suggesting toughening by TiC [15]. Fig. 13(b) shows the fracture toughness as

22   a function of the Si content in the alloy from the same data as that were used in Fig. 13(a). A

23   singular data point in the upper-right corresponds to the alloy reported by Schneibel et al., which

24   was prepared by hot isostatic pressing from Mo–20Si–10B (atom %) powder [27]. Because the

1 powder had been processed to deplete Si in its surface, the actual Si content of the alloy was less

2 than 20% and the alloy had a coarse Mo matrix although the volume fraction of Mo_{ss} phase was

3 only of the order of 30%. As indicated by the dashed lines in the Fig. 13(b), the fracture toughness

4 tends to decrease with increasing Si content in the alloy system. This is mainly due to two reasons:

5 addition of Si leads to (i) the embrittlement of the Mo_{ss} phase, and (ii) to the formation of brittle

6 silicides such as Mo_3Si, Mo_5Si_3 or T_2 [18]. The Mo–28Ti–14Si–6C–6B alloy, containing 14% Si,

7 shows a superior room-temperature fracture toughness supporting this trend. Since Si is also an

8 important element for forming a protective oxide scale on Mo–Si–B-based alloys, the Mo_{ss}–T_2–

9 Ti_5Si_3–TiC four-phase system investigated in this study shows a great potential for achieving both,

10 reasonable oxidation resistance and high room-temperature fracture toughness, in addition to

11 excellent high-temperature strength.

12

13 **4. Conclusions**

14   The microstructure, oxidation resistance, creep strength and room-temperature fracture

15 toughness of Mo–28Ti–14Si–6C–6B (atom %) alloy were systematically investigated. The alloy

16 was found to consist of four phases: Mo_{ss}, Mo_5SiB_2, Ti_5Si_3, and TiC and, therefore, incorporates

17 two recent paradigms for the design of Mo–Si–B-based alloys: TiC addition and Ti microalloying.

18 Although the alloy still exhibited catastrophic oxidation behavior at 800 °C, reasonable oxidation

19 resistance was provided by the formation of top TiO_2 and TiO_2/SiO_2 duplex oxide layers at 1100

20 and 1200 °C. Besides, the alloy exhibited a better creep strength than that of single-crystal Ni-

21 based superalloys or ternary Mo–Si–B alloys. The room-temperature fracture toughness of the

22 alloy was determined to be (12.8 ± 1.2) MPa(m)$^{1/2}$, which is superior to other Mo–Si–B-based

23 alloys considering the relatively high Si concentration in the alloy. Because the alloy possesses a

24 good balance of material properties, its design presented here is promising. Microstructure

1   refinement is expected to further enhance the fracture toughness and oxidation resistance and to

2   suppress the cracking in the T_2 phase during creep deformation.

3

11

1 **References**

2 [1] D.M. Dimiduk, J.H. Perepezko, Mo-Si-B Alloys: Developing a Revolutionary Turbine-

3   Engine Material, MRS Bull. 28 (2003) 639–645. https://doi.org/10.1557/mrs2003.191.

4 [2] J.H. Perepezko, The hotter the engine, the better, Science (80-.). 326 (2009) 1068–1069.

5   https://doi.org/10.1126/science.1179327.

6 [3] J.A. Lemberg, R.O. Ritchie, Mo-Si-B alloys for ultrahigh-temperature structural

7   applications, Adv. Mater. 24 (2012) 3445–3480.

8   https://doi.org/10.1002/adma.201200764.

9 [4] T.M. Pollock, Alloy design for aircraft engines, Nat. Mater. 15 (2016) 809–815.

10   https://doi.org/10.1038/nmat4709.

11 [5] A.P. Alur, N. Chollacoop, K.S. Kumar, High-temperature compression behavior of Mo-

12   Si-B alloys, Acta Mater. 52 (2004) 5571–5587.

13   https://doi.org/10.1016/j.actamat.2004.08.035.

14 [6] P. Jain, K.S. Kumar, Tensile creep of Mo–Si–B alloys, Acta Mater. 58 (2010) 2124–

15   2142. https://doi.org/10.1016/j.actamat.2009.11.054.

16 [7] C. Hochmuth, D. Schliephake, R. Völkl, M. Heilmaier, U. Glatzel, Influence of

17   zirconium content on microstructure and creep properties of Mo-9Si-8B alloys,

18   Intermetallics. 48 (2014) 3–9. https://doi.org/10.1016/j.intermet.2013.08.017.

19 [8] M. Krüger, P. Jain, K.S. Kumar, M. Heilmaier, Correlation between microstructure and

20   properties of fine grained Mo–Mo$_3$Si–Mo$_5$SiB$_2$alloys, Intermetallics. 48 (2014) 10–18.

21   https://doi.org/10.1016/j.intermet.2013.10.025.

22 [9] G. Hasemann, I. Bogomol, D. Schliephake, P.I. Loboda, M. Krüger, G. Hasemann, P.I.

23   Loboda, I. Bogomol, Microstructure and creep properties of a near-eutectic directionally

24   solidified multiphase Mo-Si-B alloy, Intermetallics. 48 (2013) 28–33.

1   https://doi.org/10.1016/j.intermet.2013.11.022.

2   [10] S. Miyamoto, K. Yoshimi, S.H. Ha, T. Kaneko, J. Nakamura, T. Sato, K. Maruyama, R.

3   Tu, T. Goto, Phase equilibria, microstructure, and high-temperature strength of TiC-

4   added Mo-Si-B alloys, Metall. Mater. Trans. A. 45 (2014) 1112–1123.

5   https://doi.org/10.1007/s11661-013-1779-7.

6   [11] S. Uemura, T. Yamamuro, J.W. Kim, Y. Morizono, S. Tsurekawa, K. Yoshimi,

7   Quantitative Evaluation of Microstructure in Mo-Si-B-TiC Alloy Produced by Melting

8   and Tilt Casting Methods, Mater. Trans. 59 (2018) 136–145.

9   https://doi.org/10.2320/matertrans.M2017194.

10 [12] J. Nakamura, D. Kanekon, K. Yoshimi, Characterization of Mo/Mo2C interface in

11   MoSiBTiC alloy, Mater. Lett. 180 (2016) 340–343.

12   https://doi.org/10.1016/j.matlet.2016.04.133.

13 [13] S. Yamamoto, K. Yoshimi, J. Kim, K. Yokoyama, Effects of Microstructure on High-

14   Temperature Strength of TiC-Added Mo-Si-B Alloys, Nippon Kinzoku

15   Gakkaishi/Journal Japan Inst. Met. 80 (2016) 51–59.

16   https://doi.org/10.2320/jinstmet.JB201504.

17 [14] S.Y. Kamata, D. Kanekon, Y. Lu, N. Sekido, K. Maruyama, G. Eggeler, K. Yoshimi,

18   Ultrahigh-temperature tensile creep of TiC-reinforced Mo-Si-B-based alloy, Sci. Rep. 8

19   (2018) 10487. https://doi.org/10.1038/s41598-018-28379-w.

20 [15] T. Moriyama, K. Yoshimi, M. Zhao, T. Masnou, T. Yokoyama, J. Nakamura, H. Katsui,

21   T. Goto, Room-temperature fracture toughness of MoSiBTiC alloys, Intermetallics. 84

22   (2017) 92–102. https://doi.org/10.1016/j.intermet.2017.01.004.

23 [16] M. Zhao, S. Nakayama, T. Hatakeyama, J. Nakamura, K. Yoshimi, Microstructure, high-

24   temperature deformability and oxidation resistance of a Ti_5Si_3-containing multiphase

1   MoSiBTiC alloy, Intermetallics. 90 (2017) 169–179.

2   https://doi.org/10.1016/j.intermet.2017.07.018.

3   [17]   T. Hatakeyama, N. Sekido, K. Yoshimi, Effect of Ti_5Si_3 phase on Mechanical Properties

4   and Oxidation Resistance of MoSiBTiC-based Alloys, J. Gas Turbine Soc. Japan. 46

5   (2018) 486–494.

6   [18]   S.H. Ha, K. Yoshimi, K. Maruyama, R. Tu, T. Goto, Compositional regions of single

7   phases at 1800°C in Mo-rich Mo-Si-B ternary system, Mater. Sci. Eng. A. 552 (2012)

8   179–188. https://doi.org/10.1016/j.msea.2012.05.028.

9   [19]   Y. Yang, Y.A. Chang, L. Tan, W. Cao, Multiphase equilibria in the metal-rich region of

10   the Mo-Ti-Si-B system: Thermodynamic prediction and experimental validation, Acta

11   Mater. 53 (2005) 1711–1720. https://doi.org/10.1016/j.actamat.2004.12.020.

12   [20]   Y. Yang, H. Bei, S. Chen, E.P. George, J. Tiley, Y.A. Chang, Effects of Ti, Zr, and Hf

13   on the phase stability of Mo_ss+Mo_3Si+Mo_5SiB_2 alloys at 1600°C, Acta Mater. 58

14   (2010) 541–548. https://doi.org/10.1016/j.actamat.2009.09.032.

15   [21]   R. Sakidja, J.H. Perepezko, Alloying and microstructure stability in the high-temperature

16   Mo-Si-B system, J. Nucl. Mater. 366 (2007) 407–416.

17   https://doi.org/10.1016/j.jnucmat.2007.03.029.

18   [22]   R. Sakidja, J.H. Perepezko, S. Kim, N. Sekido, Phase stability and structural defects in

19   high-temperature Mo-Si-B alloys, Acta Mater. 56 (2008) 5223–5244.

20   https://doi.org/10.1016/j.actamat.2008.07.015.

21   [23]   D. Schliephake, M. Azim, K. Von Klinski-Wetzel, B. Gorr, H.J. Christ, H. Bei, E.P.

22   George, M. Heilmaier, High-temperature creep and oxidation behavior of Mo-Si-B

23   alloys with high Ti contents, Metall. Mater. Trans. A. 45 (2014) 1102–1111.

24   https://doi.org/10.1007/s11661-013-1944-z.

1 [24] M.A. Azim, D. Schliephake, C. Hochmuth, B. Gorr, H.-J. Christ, U. Glatzel, M.

2   Heilmaier, Creep Resistance and Oxidation Behavior of Novel Mo-Si-B-Ti Alloys, JOM.

3   67 (2015) 2621–2628. https://doi.org/10.1007/s11837-015-1560-z.

4 [25] T. Hatakeyama, N. Sekido, K. Yoshimi, Effect of Cr addition on microstructure and

5   oxidation resistance of a Ti_5Si_3-containing MoSiBTiC alloy, Corros. Sci. 166 (2020)

6   108418. https://doi.org/10.1016/j.corsci.2019.108418.

7 [26] M. Zhao, K. Yoshimi, K. Maruyama, K. Yubuta, Thermal vacancy behavior analysis

8   through thermal expansion, lattice parameter and elastic modulus measurements of B2-

9   type FeAl, Acta Mater. 64 (2014) 382–390.

10   https://doi.org/10.1016/j.actamat.2013.10.051.

11 [27] J.H. Schneibel, M.J. Kramer, D.S. Easton, A Mo-Si-B intermetallic alloy with a

12   continuous α-Mo matrix, Scr. Mater. 46 (2002) 217–221. https://doi.org/10.1016/S1359-

13   6462(01)01227-1.

14 [28] Y. Yang, H. Bei, J. Tiley, E.P. George, Re effects on phase stability and mechanical

15   properties of Mo SS+Mo_3Si+Mo5SiB2 alloys, J. Alloys Compd. 556 (2013) 32–38.

16   https://doi.org/10.1016/j.jallcom.2012.12.047.

17 [29] J.J. Williams, Y.Y. Ye, M.J. Kramer, K.M. Ho, L. Hong, C.L. Fu, S.K. Malik,

18   Theoretical calculations and experimental measurements of the structure of $Ti_5Si_3$with

19   interstitial additions, Intermetallics. 8 (2000) 937–943. https://doi.org/10.1016/S0966-

20   9795(00)00064-9.

21 [30] S. Ida, N. Sekido, K. Yoshimi, Solidification pathways and phase equilibria in the Mo-

22   Ti-C ternary system, High Temp. Mater. Process. 39 (2020) 164–170.

23   https://doi.org/10.1515/htmp-2020-0053.

24 [31] M.G. Mendiratta, T.A. Parthasarathy, D.M. Dimiduk, Oxidation behavior of αMo-

1   Mo3Si-Mo $_5$SiB $_2$ (T2) three phase system, Intermetallics. 10 (2002) 225–232.

2   https://doi.org/10.1016/S0966-9795(01)00118-2.

3 [32] T.A. Parthasarathy, M.G. Mendiratta, D.M. Dimiduk, Oxidation mechanisms in Mo-

4   reinforced $Mo_5SiB_2(T_2)$-Mo_3Si alloys, Acta Mater. 50 (2002) 1857–1868.

5   https://doi.org/10.1016/S1359-6454(02)00039-3.

6 [33] M. Azimovna Azim, S. Burk, B. Gorr, H.J. Christ, D. Schliephake, M. Heilmaier, R.

7   Bornemann, P.H. Bolívar, Effect of Ti (Macro-) alloying on the high-temperature

8   oxidation behavior of ternary Mo-Si-B alloys at 820-1,300 C, Oxid. Met. 80 (2013) 231–

9   242. https://doi.org/10.1007/s11085-013-9375-1.

10 [34] M. Zhao, B. Xu, Y. Shao, J. Liang, S. Wu, Y. Yan, Oxidation behavior of Mo_{ss}–Ti_5Si_3–

11   T_2 composites at intermediate and high temperatures, Intermetallics. 118 (2020) 106702.

12   https://doi.org/10.1016/j.intermet.2020.106702.

13 [35] S. Majumdar, B. Paul, P.K. Singh, J. Kishor, V. Kain, Effect of Si content on

14   microstructure, mechanical and oxidation properties of hot pressed Mo-Ti-Si alloys,

15   Intermetallics. 100 (2018) 126–135. https://doi.org/10.1016/j.intermet.2018.06.013.

16 [36] F.A. Rioult, S.D. Imhoff, R. Sakidja, J.H. Perepezko, Transient oxidation of Mo-Si-B

17   alloys: Effect of the microstructure size scale, Acta Mater. 57 (2009) 4600–4613.

18   https://doi.org/10.1016/j.actamat.2009.06.036.

19 [37] D. Schliephake, A. Kauffmann, X. Cong, C. Gombola, M. Azim, B. Gorr, H.J. Christ,

20   M. Heilmaier, Constitution, oxidation and creep of eutectic and eutectoid Mo-Si-Ti

21   alloys, Intermetallics. 104 (2019) 133–142.

22   https://doi.org/10.1016/j.intermet.2018.10.028.

23 [38] S. Obert, A. Kauffmann, M. Heilmaier, Characterisation of the oxidation and creep

24   behaviour of novel Mo-Si-Ti alloys, Acta Mater. 184 (2020) 132–142.

1   https://doi.org/10.1016/j.actamat.2019.11.045.

2   [39] S. Obert, A. Kauffmann, S. Seils, S. Schellert, M. Weber, B. Gorr, H.-J. Christ, M.

3   Heilmaier, On the chemical and microstructural requirements for the pesting-resistance

4   of Mo–Si–Ti alloys, J. Mater. Res. Technol. 9 (2020) 8556–8567.

5   https://doi.org/10.1016/j.jmrt.2020.06.002.

6   [40] T. Hatakeyama, S. Ida, N. Sekido, K. Yoshimi, Significant improvement of the oxidation

7   resistance of MoSiBTiC-based multiphase alloys by Ti enrichment, Corros. Sci. 176

8   (2020). https://doi.org/10.1016/j.corsci.2020.108937.

9   [41] K. Sadananda, C.R. Feng, R. Mitra, S.C. Deevi, Creep and fatigue properties of high

10   temperature silicides and their composites, Mater. Sci. Eng. A. 261 (1999) 223–238.

11   https://doi.org/10.1016/s0921-5093(98)01070-3.

12   [42] M. Heilmaier, M. Krüger, H. Saage, J. Rösler, D. Mukherji, U. Glatzel, R. Völkl, R.

13   Hüttner, G. Eggeler, C. Somsen, T. Depka, H.J. Christ, B. Gorr, S. Burk, Metallic

14   materials for structural applications beyond nickel-based superalloys, JOM. 61 (2009)

15   61–67. https://doi.org/10.1007/s11837-009-0106-7.

16   [43] J.H. Schneibel, R.O. Ritchie, J.J. Kruzic, P.F. Tortorelli, Optimizaton of Mo-Si-B

17   intermetallic alloys, Metall. Mater. Trans. A Phys. Metall. Mater. Sci. 36 (2005) 525–

18   531. https://doi.org/10.1007/s11661-005-0166-4.

19   [44] D. Sturm, M. Heilmaier, J.H. Schneibel, P. Jéhanno, B. Skrotzki, H. Saage, The

20   influence of silicon on the strength and fracture toughness of molybdenum, Mater. Sci.

21   Eng. A. 463 (2007) 107–114. https://doi.org/10.1016/j.msea.2006.07.153.

22   [45] H. Okamoto, Mo-Si (Molybdenum-Silicon), J. Phase Equilibria Diffus. 32 (2011) 176.

23   https://doi.org/10.1007/s11669-010-9843-0.

24   [46] K. Ihara, K. Ito, K. Tanaka, M. Yamaguchi, Mechanical properties of Mo_5SiB_2 single

1   crystals, Mater. Sci. Eng. A. 329–331 (2002) 222–227. https://doi.org/10.1016/S0921-

2   5093(01)01575-1.

3   [47] M.F. Ashby, F.J. Blunt, M. Bannister, Flow characteristics of highly constrained metal

4   wires, Acta Metall. 37 (1989) 1847–1857. https://doi.org/10.1016/0001-6160(89)90069-

5   2.

6   [48] H. Fukuyama, R. Sawada, H. Nakashima, M. Ohtsuka, K. Yoshimi, Study of

7   solidification pathway of a MoSiBTiC alloy by optical thermal analysis and in-situ

8   observation with electromagnetic levitation, Sci. Rep. 9 (2019) 15049.

9   https://doi.org/10.1038/s41598-019-50945-z.

10 [49] S. Uemura, S.Y. Kamata, K. Yoshimi, Microstructural Evolution during High-

11   Temperature Tensile Creep at 1500°C of a MoSiBTiC Alloy, High Temp. Mater.

12   Process. 39 (2020) 136–145.

13
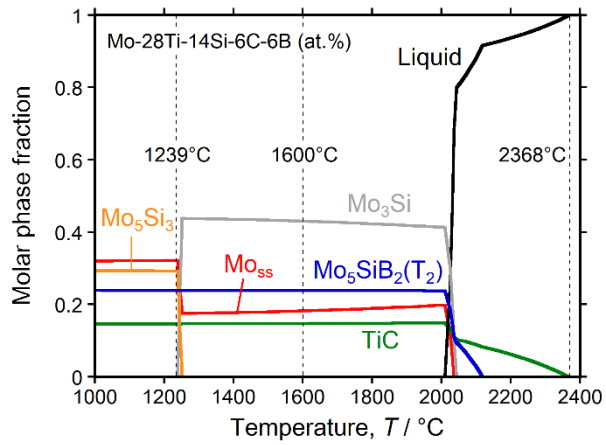
1

2 **Figure 01** Molar phase fractions obtained by thermodynamic calculations for equilibrium as a

3 function of temperature. (Color on the web and black-and-white in print)

4
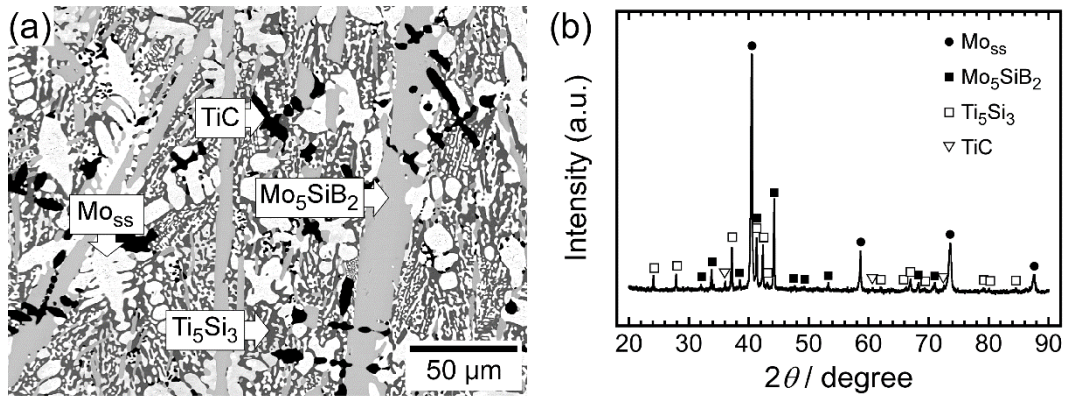
1

2 **Figure 02** Mo–28Ti–14Si–6C–6B alloy heat treated at 1600 °C for 24 hours: (a) BSE image of

3 the initial microstructure and (b) XRD pattern.

4

1
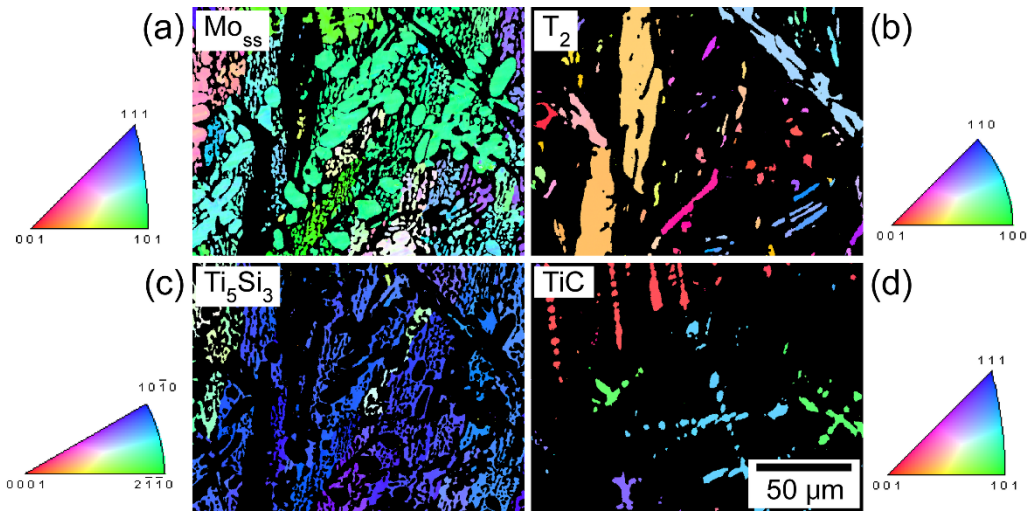
2

3   **Figure 03** IPF maps of (a) Mo_{ss}, (b) T_2, (c) Ti_5Si_3 and (d) TiC within the Mo–28Ti–14Si–6C–6B

4   alloy after casting and heat-treatment. (Color on the web and in print)

5

1
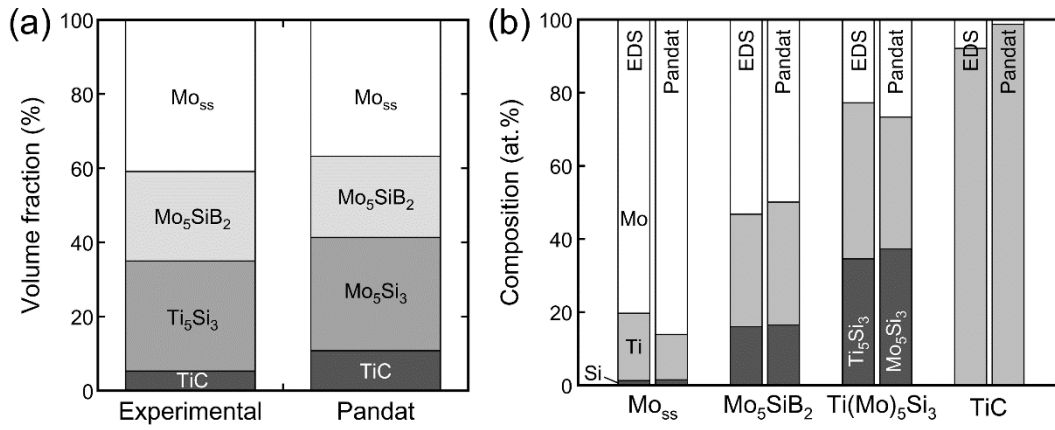
Figure 04 Experimentally and thermodynamically determined (a) volume fraction and (b) compositions of the constituent phases in the Mo–28Ti–14Si–6C–6B alloy.

5
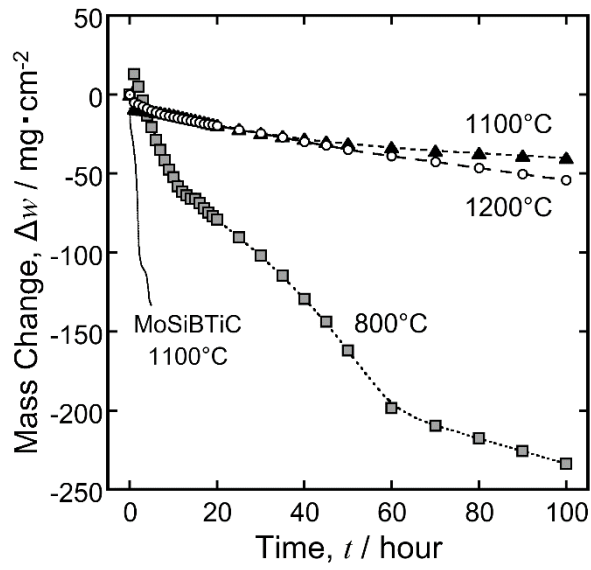
Figure 05 Cyclic oxidation kinetics of the Mo–28Ti–14Si–6C–6B alloy determined at 800, 1100

and 1200 °C. The isothermal kinetics of the 1st generation Mo–Si–B–TiC alloy at 1100 °C, as

reported by Zhao et al. [16], are included for comparison.
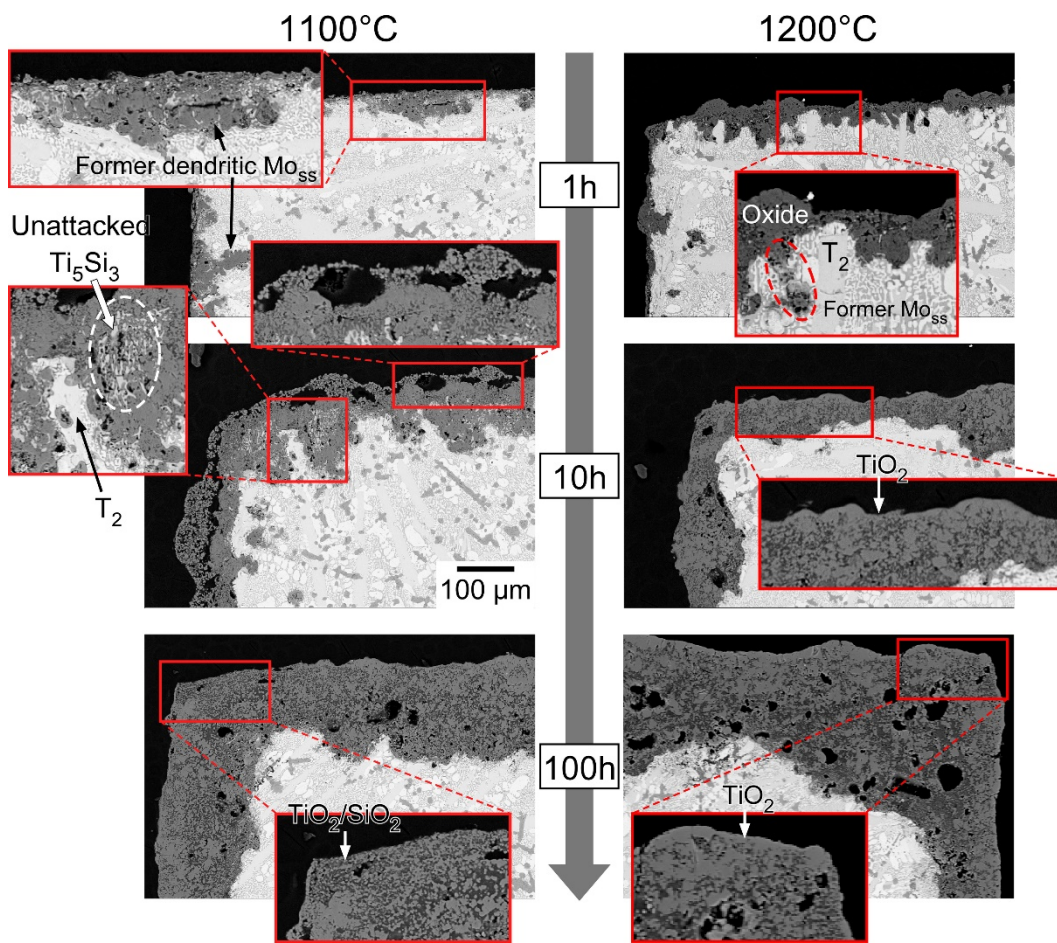
Figure 06 BSE images of the cross-sections of the Mo–28Ti–14Si–6C–6B alloy oxidized for 1, 10 and 100 h under cyclic conditions at 1100 and 1200 °C in air. (Color on the web and black-and-white in print)
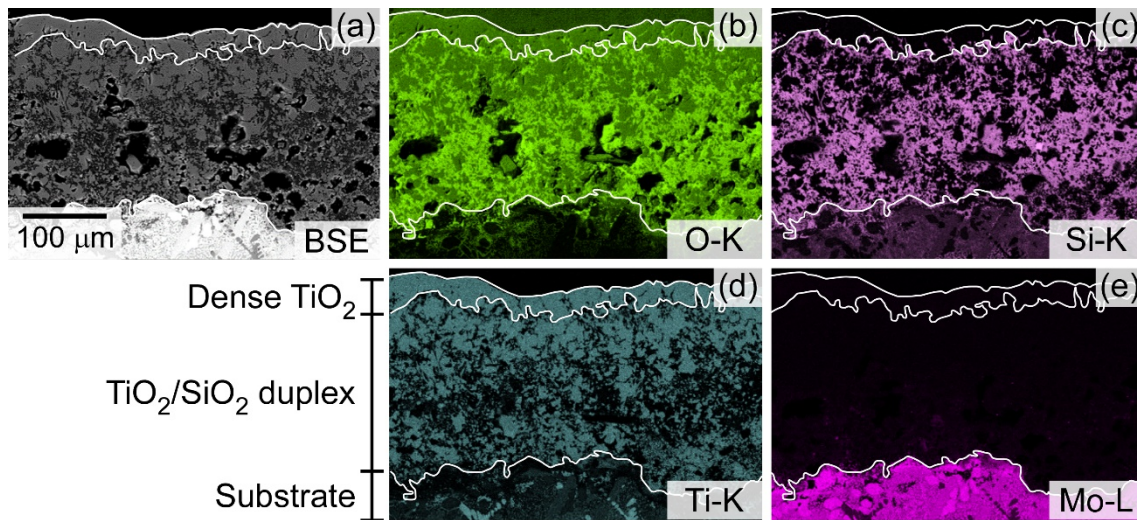
Figure 07 (a) BSE image of the cross-section of the alloy oxidized at 1200 °C for 100 h and the corresponding EDS elemental mappings of (b) O, (c) Si, (d) Ti and (e) Mo. (Color on the web and black-and-white in print)
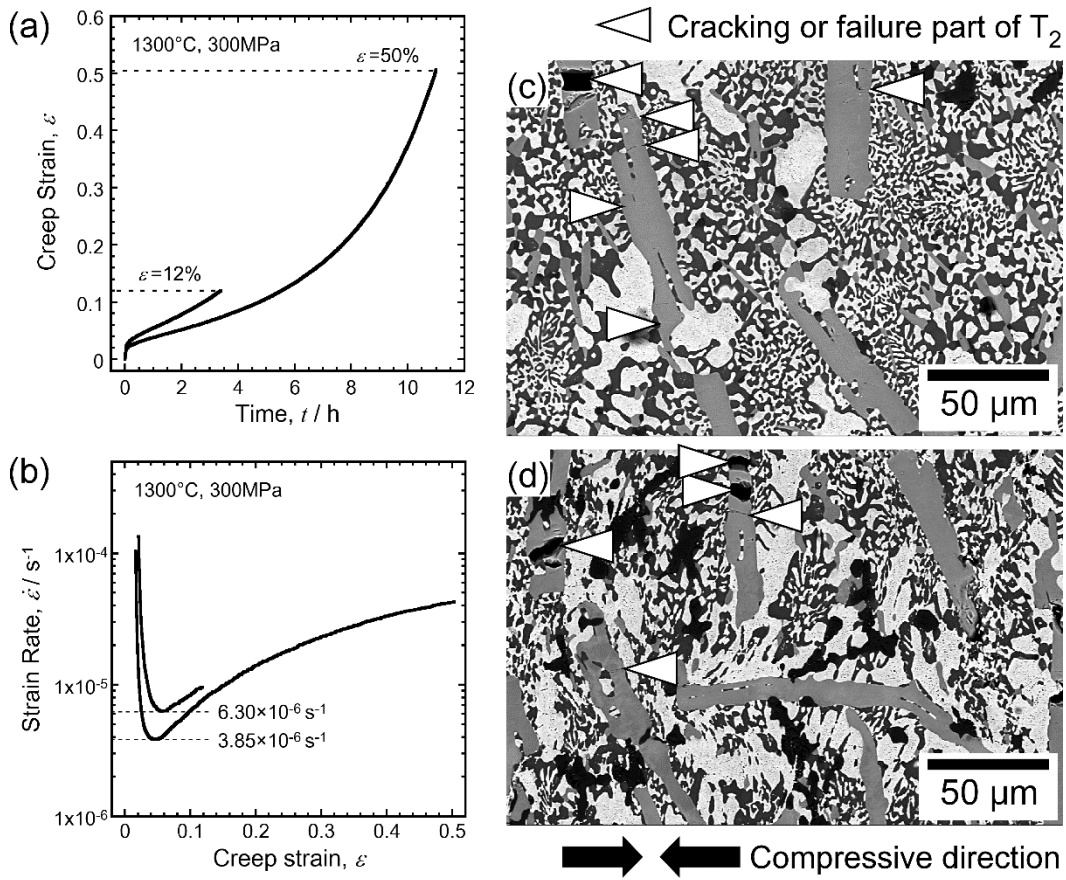
Figure 08 (a) Creep strain versus time curve, (b) strain rate versus creep strain curve obtained at

1300 °C and 300 MPa and the microstructure of the alloy after compression creep testing to

logarithmic strains of (c) 12% and (d) 50%.
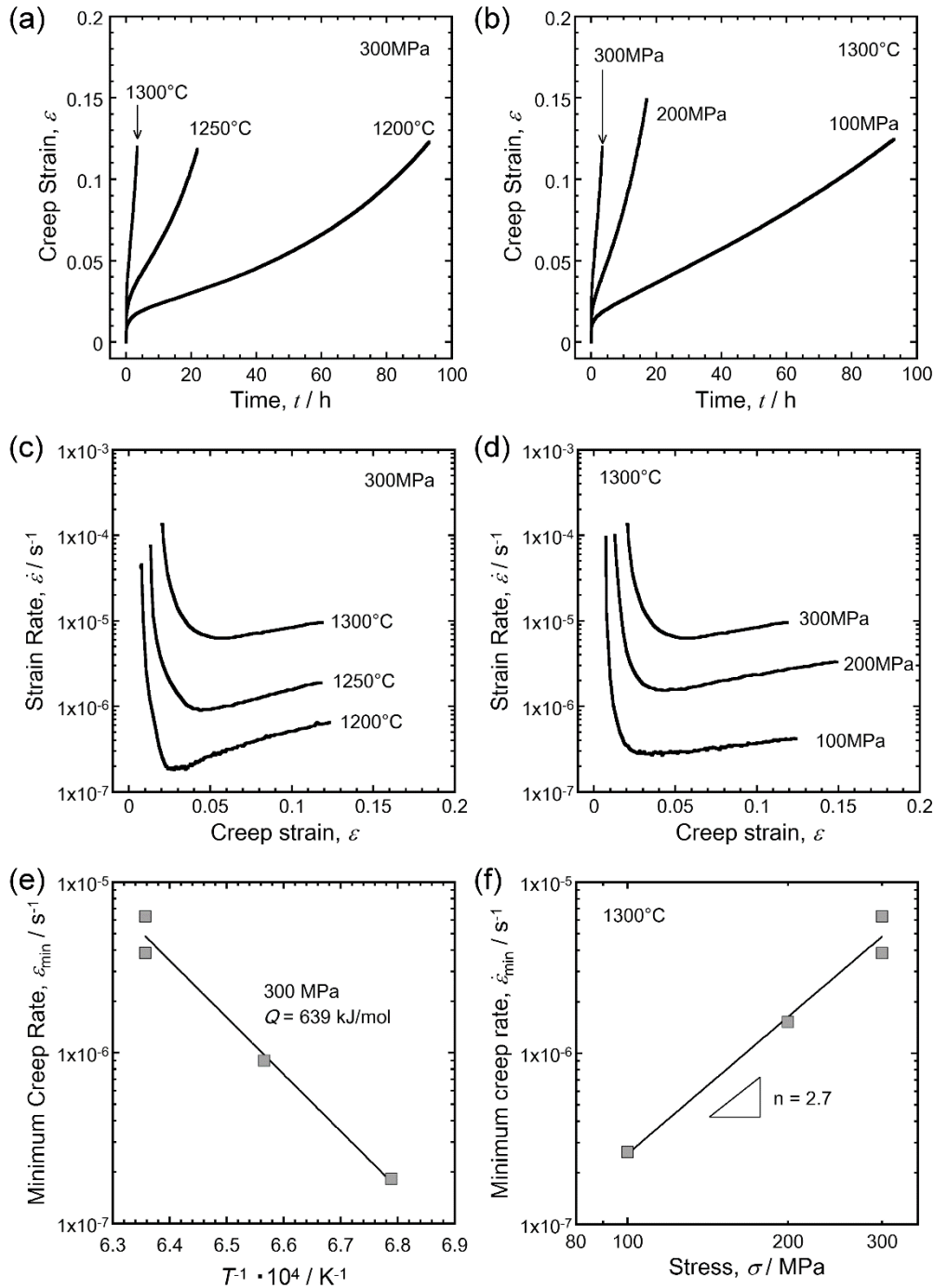
Figure 09 Compressive creep-strain versus time curves obtained at (a) 1200–1300 °C and 300 MPa, (b) 1300 °C and 100–300 MPa; strain-rate versus creep-strain curves obtained at (c) 1200–1300 °C and 300 MPa, (d) 1300 °C and 100–300 MPa, (e) Arrhenius plot of the minimum creep-rate (s^{-1}) as a function of the inverse temperature (K^{-1}) and (f) a Norton plot of the minimum creep-rate (s^{-1}) as a function of stress (MPa) in a log–log plot.
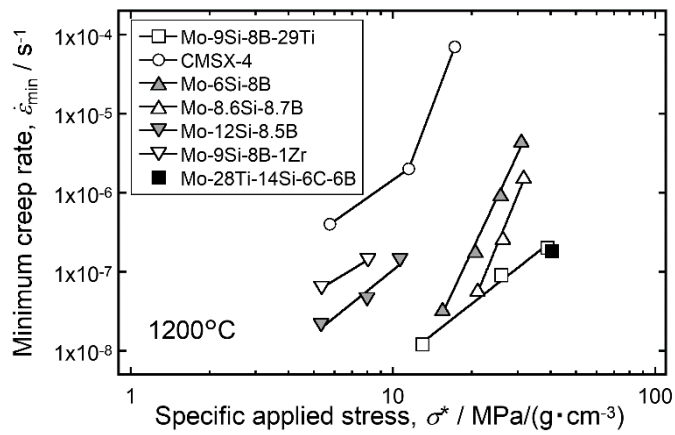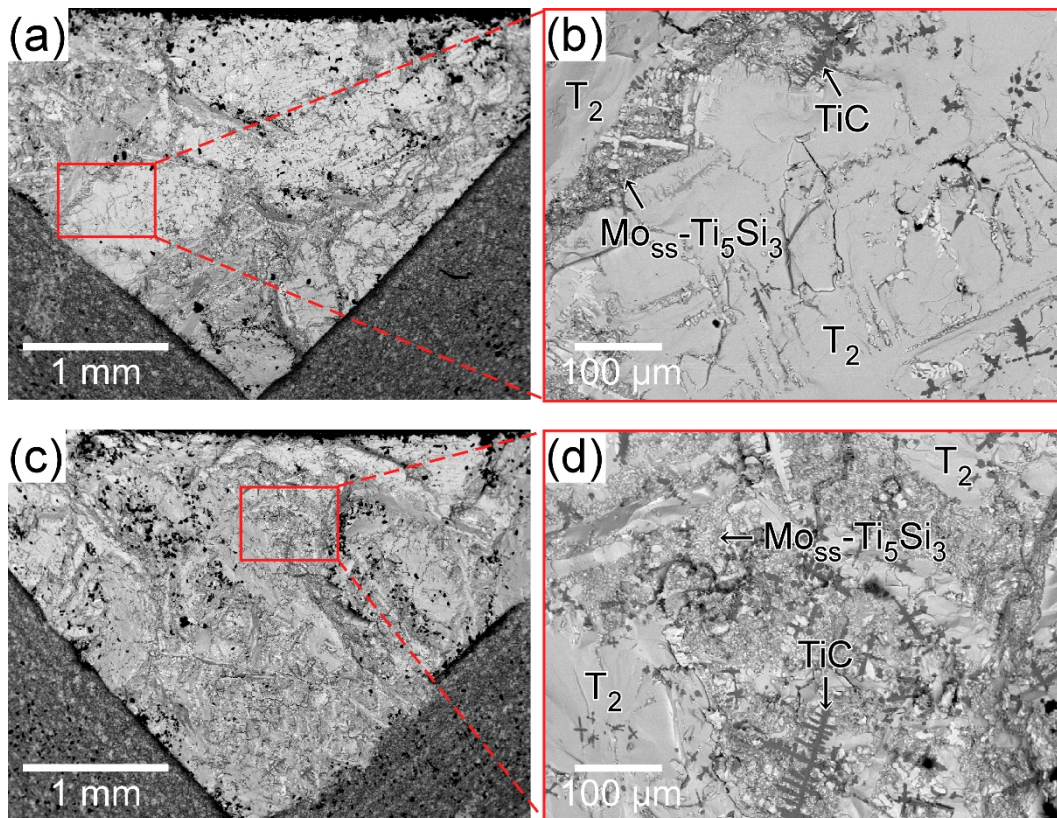
Figure 10 Double logarithmic plot of the minimum creep rate against applied stress at 1200 °C

and 300 MPa compared with those of other Mo–Si–B alloys and the single-crystal Ni-based

superalloy CMSX-4 [6,23,41,42].
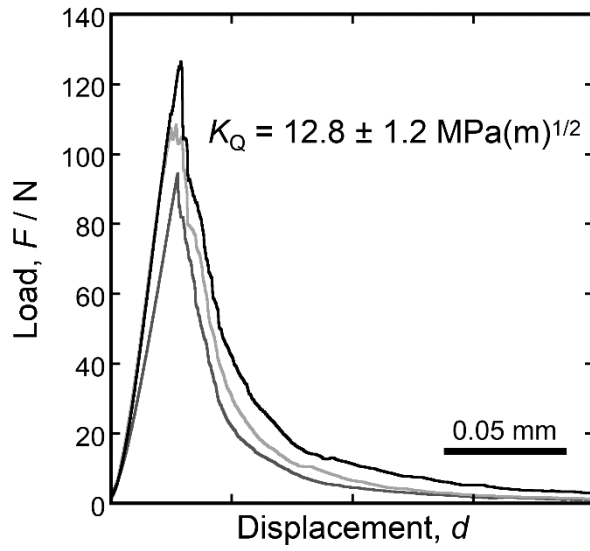
$K_Q = 12.8 \pm 1.2 \text{ MPa(m)}^{1/2}$

Figure 11 Load–displacement curves for heat-treated Mo–28Ti–14Si–6C–6B alloy in a three-point bending test.
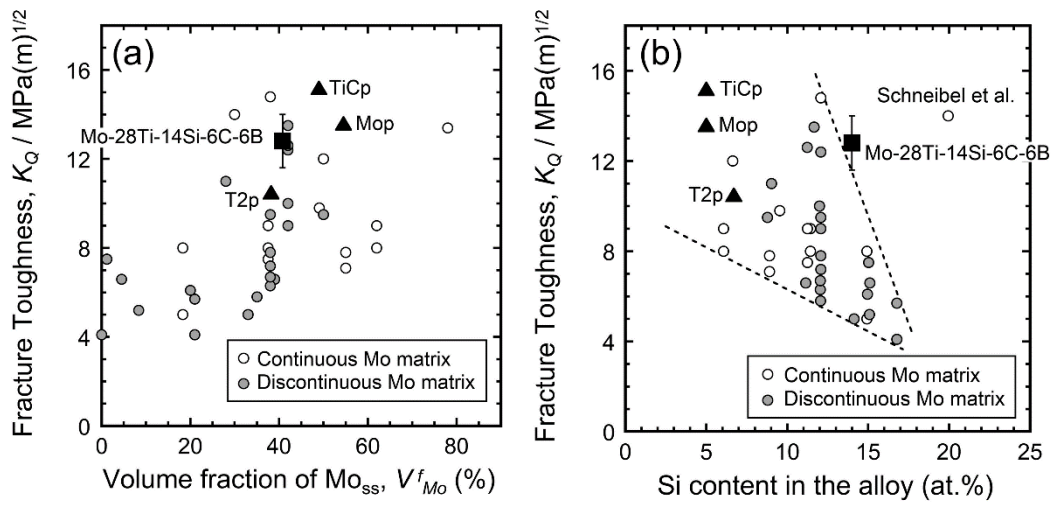
Figure 12 SEM-BSE images of the fracture surfaces of the alloy after a three-point bending test.

(b) and (d) are higher magnification images of the regions indicated in (a) and (c), respectively.

(Color on the web and black-and-white in print)

Figure 13 Comparison of the fracture toughness of TiC-added Mo–Si–B alloys (TiCp, Mop, T2p) [15] and Mo–28Ti–14Si–6C–6B alloys with data collected by Lemberg and Ritchie [3] as a function of (a) volume fraction of Mo_{ss} and (b) Si content in the alloy.